Terr. Atmos. Ocean. Sci., Vol. 30, No. 3, 285-300, June 2019 doi: 10.3319/TAO.2019.04.03.01

# Triggered slip on multifaults after the 2018 $M_w$ 6.4 Hualien earthquake by continuous GPS and InSAR measurements

Hsin Tung[1], Horng-Yue Chen[2], Ya-Ju Hsu[2], Jyr-Ching Hu[1,*], Yo-Ho Chang[3], and Yu-Ting Kuo[2]

[1] *Department of Geosciences, National Taiwan University, Taipei City, Taiwan*
[2] *Institute of Earth Sciences, Academia Sinica, Taipei City, Taiwan*
[3] *Department of Natural Resources and Environmental Studies, National Dong Hwa University, Hualien County, Taiwan*

***Article history:***
Received 13 August 2018
Revised 15 March 2019
Accepted 3 April 2019

***Keywords:***
High-rate GPS, InSAR, Multi-fault slip triggering, Peak Ground Displacement

***Citation:***
Tung, H., H.-Y. Chen, Y.-J. Hsu, J.-C. Hu, Y.-H. Chang, and Y.-T. Kuo, 2019: Triggered slip on multifaults after the 2018 $M_w$ 6.4 Hualien earthquake by continuous GPS and InSAR measurements. Terr. Atmos. Ocean. Sci., 30, 285-300, doi: 10.3319/TAO.2019.04.03.01

## ABSTRACT

On 6 February 2018 at 23:50 local time, a $M_w$ 6.4 earthquake struck eastern Taiwan. We characterize the instantaneous surface ground motion and the permanent displacement induced by this event from continuous GPS data and SAR images within a short time after the mainshock. We use high-rate GPS positioning techniques to obtain epoch-by-epoch positions peak ground displacement to assess potential seismic damage. The maximum coseismic GPS horizontal displacement of about 450 mm trending to the northeast is observed at the station HUAL located on the hanging wall of the Milun fault. The PEPU located on the footwall of the Milun fault shows a coseismic horizontal displacement of 280 mm trending to the southwest and a coseismic uplift of about 70 mm. Moreover, ascending and descending tracks of ALOS-2 and Sentinel-1 SAR images are processed to estimate coseismic surface deformation along the line-of-sight (LOS) toward the satellite. Then, wide coverage from east-west and uplift components of surface deformation is fulfilled by combining the LOS displacement from ascending and descending interferograms. The main deformation area revealed by both GPS results and D-InSAR interferograms is concentrated around the Milun and Lingding faults. Significant uplift on the footwall of the northern Lingding Fault implies that the Milun fault and an unknown west-dipping fault close to the Lingding fault were triggered. Both the two nodal planes of the $M_w$ 6.4 Hualien event could be different with the kinematic behavior of the Milun fault and Lingding fault. Thus we suggest that slip on multiple faults was triggered during the 0206 event.

## 1. INTRODUCTION

At 21:56:41 local time on 4 February 2018, a $M_w$ 6.0 (0204 event) occurred in the Hsinchen Ridge offshore the city of Hualien (Fig. 1). According to the focal mechanism of this event, the possible seismogenic fault is a nearly E-W-striking and gently north-dipping thrust fault with a minor dextral strike-slip component. This event could be interpreted as a regular subduction zone earthquake that occurred at the complex junction of convergence boundary of the Philippine Sea plate and Eurasian plate. Two days later, a $M_w$ 6.4 earthquake (0206 event) occurred near the epicenter of 0204 event with a different focal mechanism. The epicenter of this second event was located in the offshore area ~16.5 km northeast of city of Hualien at a depth of 6 km resulting in 17 deaths with 285 injured. Based on the Central Weather Bureau (CWB) intensity scale, the peak ground acceleration (PGA) larger than 400 gals were measured in Hualien. This extremely large ground shaking caused severe building damage, including four that had partially collapsed. Thousands of aftershocks were recorded by Geophysical Database Management System (https://gdms.cwb.gov.tw/index.php) of CWB within 14 days (Kuo-Chen et al. 2019). Aftershocks were propagated southward from the hypocenter of the mainshock to the Longitudinal Valley (Chang et al. 2019; Chen et al. 2019).

According to field investigations, the major surface rupture was identified along the Milun fault (Huang et al. 2019; Lin et al. 2019; Wu et al. 2019), an active fault that

* *Corresponding author*
*E-mail: jchu@ntu.edu.tw*

ruptured during a $M_L$ 7.1 earthquake in 1951 (Hsu 1962, 1971; Bonilla 1975, 1977). Based on the focal mechanism solution, a NE-striking and NW-dipping nodal plane is considered as the seismogenic fault plane indicating a reverse faulting with a sinistral strike-slip component. An alternative nodal plane is close to a EW-striking south-dipping reverse fault with dextral slip component. However, both these two nodal plane are hard to connect to any known active fault near the epicenter. Furthermore, the coseismic deformation patterns revealed by continuous GPS measurements and SAR interferograms were observed both on the hanging wall and footwall of the Milun fault, which is a NE-striking and east-dipping reverse fault with a sinistral motion based on geological data (e.g., Shyu et al. 2005). In addition, significant coseismic deformation behavior also observed on the footwall part of the Lingding fault which is the northern segment of the Longitudinal Valley fault, suggesting that the 0206 Hualien earthquake triggered multiple ruptures on different fault systems (Huang and Huang 2018; Yang et al. 2018), similar to multiple fault slip founded during the 2010 $M_w$ 6.2 Jia-Shian earthquake (Lin et al. 2016), the 2016 $M_w$ 6.4 Meinong earthquake in southern Taiwan (Huang et al. 2016; Le Béon et al. 2017) and the 2016 $M_w$ 7.8 Kaikōura earthquake in New Zealand (Hamling et al. 2017). The shallow rupture of the Milun fault and its kinematic behavior are also revealed by optical satellite and numerical modeling (Kuo et al. 2019). They proposed the different locking depth and kinematic behavior in the north and south segment of the Milun fault. In addition, the detailed insights of seismogenic deformation near the Milun fault by 3D displacement field by GPS, InSAR and pixel offsets from ALOS-2 radar image are deduced to suggest the Milun and Lingding faults belong to same fault zone (Yen et al. 2019). The coseismic deformation also conducted by using strong motion recordings (Tian et al. 2019). They indicated that the Milun fault could have experienced a left-lateral motion during the Hualien event.

To better characterize coseismic deformation of multiple fault slip triggered by the 0206 offshore Hualien earthquake, we use continuous GPS (cGPS) data from the Taiwan cGPS array and 12 cGPS sites operated by the NDHU to estimate the coseismic displacement around the epicenter as well as along the Milun and Lingding fault systems. In addition, differential interferometry synthetic aperture radar (D-InSAR) technique from ALOS-2 and Sentinel-1 radar images are used to characterize coseismic deformation

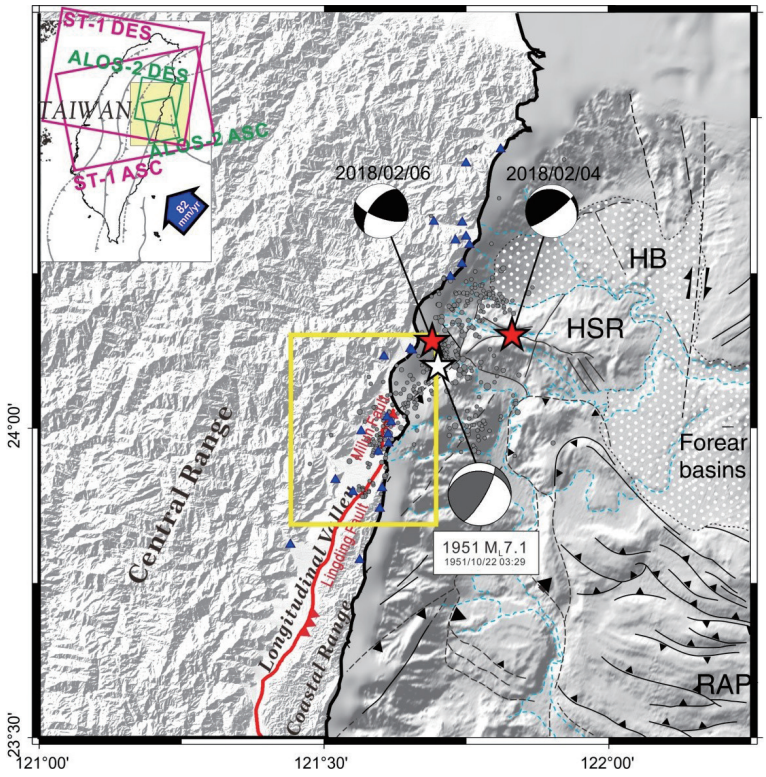


Fig. 1. Locations for continuous GPS stations (blue triangles), SAR coverage (rectangle) and focal mechanism of the 2018 0204 $M_w$ 6.0 and 0206 $M_w$ 6.4 earthquakes in Taiwan. White star is the $M_L$ 7.1 event of the 1951 Hualien-Taitung earthquake sequence, and gray circles are the aftershocks occurred within two weeks after the 0206 event. Yellow rectangle indicates study area. ASC represents ascending orbit while DES represents descending orbit. ST-1 represents Sentinel-1 satellite. Blue arrow shows the plate convergence rate between the Philippines Sea plate and Eurasian plate (after Lin et al. 2010). Offshore bathymetry and tectonic structures are based on Malavieille et al. (2002). HSR represents Hsinchen Ridge, HB represents Hoping Basin, and RAP indicates Ryukyu Accretionary Prism.

patterns and fault ruptures associated with the mainshock. Furthermore, high-rate GPS data (1 Hz sampling rate) of cGPS are used to estimate the peak ground displacement (PGD) adjacent to the hypocenter for assessing the potential seismic damage. Finally, we calculate the arrival time of the PGD from cGPS stations to infer the multiple fault slip triggered by the $M_w$ 6.4 event.

Although there are several papers have been published using geodetic data such as campaign GPS, InSAR, precise leveling and pixel offtrack techniques based on optical and SAR images to explain the coseismic deformation and to inverse the coseismic slip on patches of the seismogenic fault or triggered fault systems. However, all these geodetic results might be contaminated by interseismic and postseismic displacements. In this paper, we provide both instantaneous surface ground motion and the permanent displacement from continuous high-rate GPS data within a short time after the event with detail processing strategy. We also provide reliable high-rate GPS waveforms which could be used for time-dependent modeling of this event for the future study.

## 2. DATA ACQUISITION AND PROCESSING

To study the instantaneous surface ground motion and the permanent displacement caused by the earthquake, we used GPS observations and SAR images to measure precise positioning coordinates and the differential movements around the epicenter. GPS data provide a nice temporal resolution for the rupture process where as SAR images offer a better spatial coverage of deformation pattern.

### 2.1 GPS Observations

Taiwan's cGPS array is one of the densest GPS networks in the world. There are more than 400 stations over an area of 36000 km$^2$ (Tsai et al. 2015). To enhance the near real-time applications, internet transmission and latest generation dual-frequency receiver with multi-satellites recording function were installed in most stations. The data are mainly collected by the Central Weather Bureau (CWB), the Ministry of Interior Affairs (MOI), the Institute of Earth Sciences, Academia Sinica (IESAS), the Central Geological Survey (CGS), and the Water Resources Agency (WRA). Furthermore, the National Dong Hwa University also provides GPS data in Hualien (Fig. 1). In order to precisely determine the coseismic displacement and surface ground motion, we collected cGPS data from 1st to 11th February with sampling rate of 30-s to estimate instantaneous positioning and daily solutions, respectively (Fig. 2). Furthermore, high-rate GPS positioning techniques have been developed to obtain epoch-by-epoch positions and these solutions are capable of recording seismic motion acting as GPS Seismology (e.g., Nikolaidis et al. 2001; Bock et al. 2004). In this study, 1 Hz sampling rate data of cGPS are used both to estimate the instantaneous positioning (Fig. 2) and PGD of the GPS station for assessing the potential seismic damage (detail in discussion).

We utilize the GIPSY-OASIS II software (Webb and

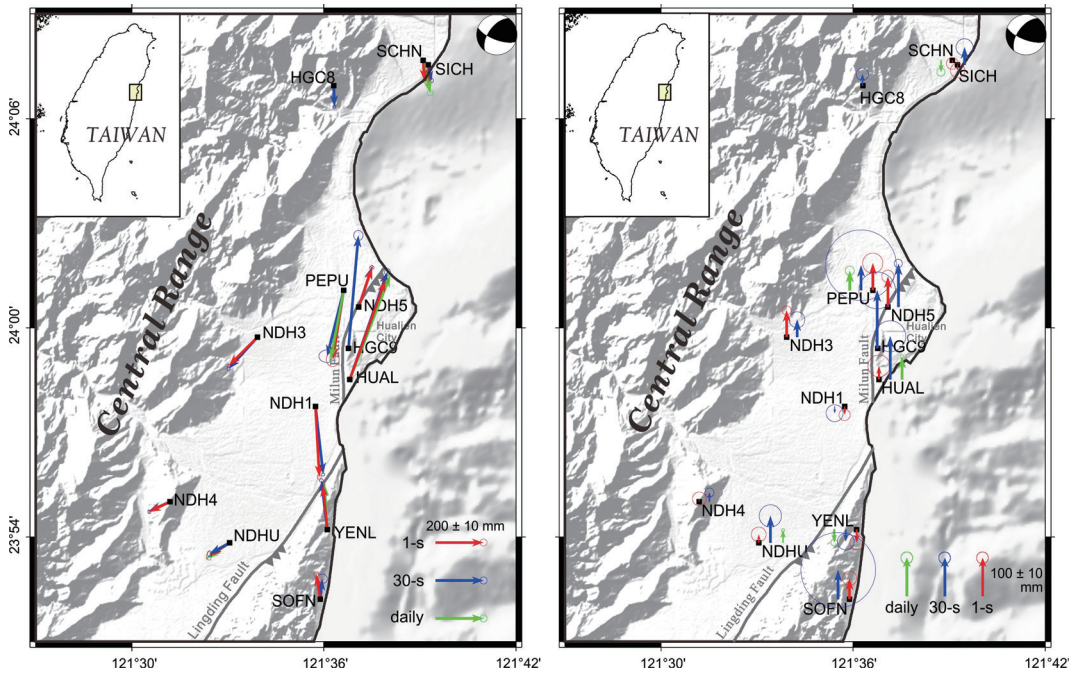


Fig. 2. Coseismic displacements of cGPS stations for the $M_w$ 6.4 Hualien earthquake. Blue arrows represent position difference using the average of 30-s solutions 60 min prior to and post the mainshock; red arrows represent 1-hz solutions using 60 s GPS before and after the mainshock, and green arrows represent position differences between the averages GPS positions 5 days prior to and post the mainshock.

Zumberge 1997) to estimate the coordinates in precise point positioning (PPP) method. The PPP technique acquires absolute position using a single GPS station, which has a lower precision than the differential technique (GAMIT from Herring et al. 2009 or Bernese from Dach et al. 2007) with the capability of removing the common errors from two or more stations. The accuracy of PPP depends on the ability of mitigating all kinds of errors. In this study, the International GNSS Service (IGS) final products were used to reduce satellite orbit and clock errors in the data procedures. Besides, Vienna Mapping Function (VMF1) and antenna calibration provided from NOAA's National Geodetic Survey were used to reduce atmosphere delay and receiver error.

### 2.2 D-InSAR

We combined both ALOS-2 and Sentinel-1 ascending and descending SAR data to measure the coseismic deformation fields of the Hualian earthquake. Table 1 presents the detailed information of the used SAR data, and the coverage of the four tracks is shown in Fig. 1. After the 0206 event, Advanced Land Observing Satellite-2 (ALOS-2) launched by Japan Aerospace Exploration Agency (JAXA) passed over the Hualien area on 10 and 11 February for emergency observation with stripmap mode SAR images. Thus, one ascending interferogram (2016/11/05 - 2018/02/10) and one descending interferogram (2017/06/18 - 2018/02/11) could be generated with two historical images. In addition, Sentinel-1 satellite constellation launched by the European Space Agency (ESA) also provided Wide (IW) mode ascending and descending images in 3 days and 5 days after the 0206 event, respectively. After that, two interferograms with a six-days interval could be generated (2018/02/03 - 2018/02/09 for ascending pair and 2018/02/05 - 2018/02/11 for descending pair). The four interferograms were generated using the ISCE (InSAR Scientific Computing Environment) software developed by the JPL/Caltech (Rosen et al. 2012). One-arc-second resolution Shuttle Radar Topography Mission (SRTM) digital elevation model (Farr et al. 2007) was used to remove the topography phase component during interferogram processing to estimate surface deformation in the area covering the Milun fault and the northern part of the Lingding fault (Fig. 3). Finally, Snaphu version 1.4.2 (Chen and Zebker 2000) has been applied to process phase unwrapping (Fig. 4).

## 3. COSEISMIC DISPLACEMENT OBSERVED FROM CGPS AND D-INSAR

GPS observations and SAR interferograms can be used to estimate coseismic displacements at different time scales. First, we use GPS daily solution and 1 Hz sampling data to determine the coseismic deformation. Second, we use D-InSAR technique with Sentinel-1 and ALOS-2 images to evaluate the regional deformation patterns over a week after the mainshock and over a longer time period which might include both coseismic and postseismic deformation of the $M_w$ 6.4 Hualien earthquake.

### 3.1 cGPS Result

From the different precise orbit and clock products released from JPL, we estimate 3 coseismic displacement fields from (1) GPS positions difference between the averages of 30-s solutions 60 min prior to and post the mainshock with rapid orbit in two days after the 0206 event; (2) positions difference between the averages of 1-hz solutions 60 s prior to and post the mainshock; (3) difference between the averages daily solutions 5 days prior to and post the mainshock with final orbit in 14 days after the 0206 event (Fig. 2 and Table 2). Unfortunately, due to the data exchange policy and failure of power supply after the Hualien earthquake, only few GPS stations were available for estimates of daily solutions. However, the results of the 3 different processing strategies indicate similar coseismic deformation patterns observed along the Milun fault and Lingding fault (Fig. 2).

The maximum horizontal displacement is measured in the GPS station HUAL, which is sat in downtown of Hualien and hanging wall of the Milun fault, with a horizontal displacement of about 450 mm trending to northeast and varies in uplift from 35 - 115 mm. Furthermore, the GPS station NDH5 and HGC9 located on the hanging wall of the

Table 1. Parameters of differential SAR interferometric pairs of ALOS-2 and Sentinel-1 images.

| Pair | Satellite | Image Resolution (m) | Flight direction | Acquisition Date | Time Interval (days) | Heading Angle | Incidence Angle | Perpendicular Baseline (m) |
|---|---|---|---|---|---|---|---|---|
| 1 | ALOS-2<br>ALOS-2 | 6 | Ascending | 2016/11/05<br>2018/02/10 | 461 | 347.9° | 27.8° | -160.7 |
| 2 | ALOS-2<br>ALOS-2 | 10 | Descending | 2017/06/18<br>2018/02/11 | 238 | 192.1° | 40.6° | 229.2 |
| 3 | Sentinel-1A<br>Sentinel-1B | 5 × 20<br>5 × 20 | Ascending | 2018/02/03<br>2018/02/09 | 6 | 347.6° | 41.6° | -9.8 |
| 4 | Sentinel-1A<br>Sentinel-1B | 5 × 20<br>5 × 20 | Descending | 2018/02/05<br>2018/02/11 | 6 | 192.4° | 34.2° | -44.0 |

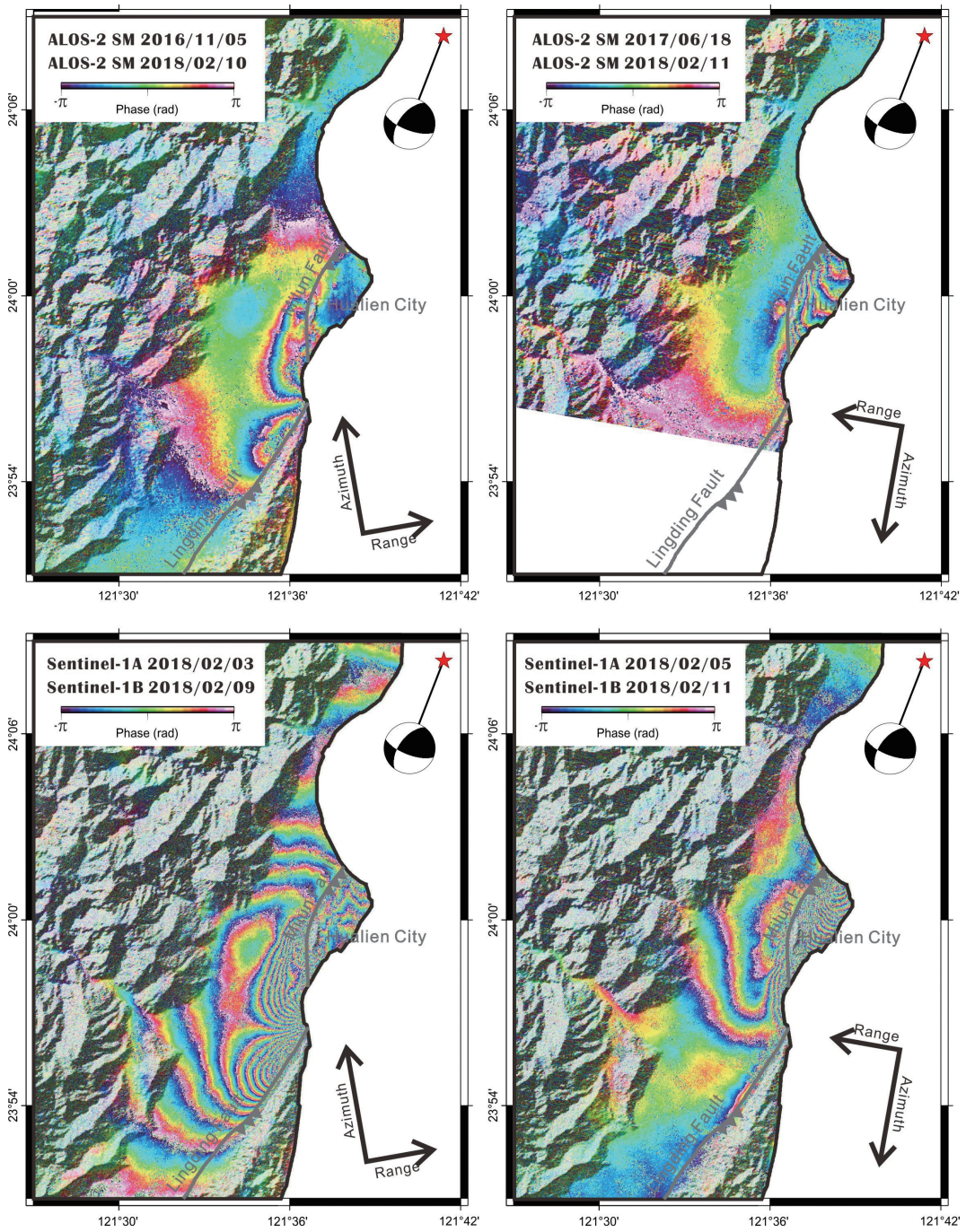


Fig. 3. Wrapped DInSAR interferograms derived from ALOS-2 (upper two figures) and Sentinel-1 radar images (lower two figures) acquired before and after the $M_w$ 6.4 Hualien Earthquake.

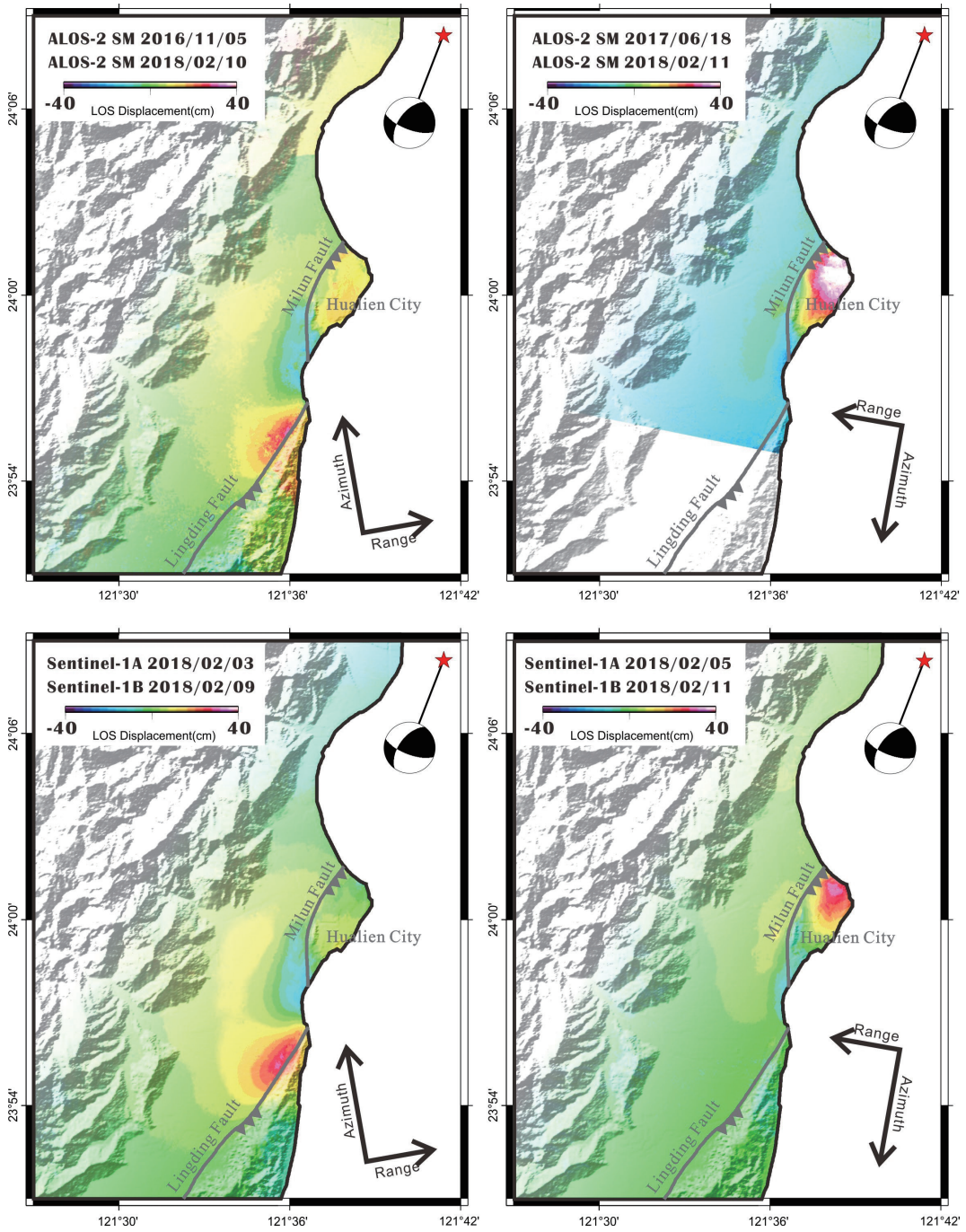


Fig. 4. Unwrapped DInSAR deformation derived from ALOS-2 (upper two figures) and Sentinel-1 radar images (lower two figures) acquired before and after the $M_w$ 6.4 Hualien Earthquake by using Snaphu version 1.4.2 (Chen and Zebker 2000).

Table 2. cGPS coseismic displacements of the $M_w$ 6.4 Hualien earthquake.

| Station | Longitude (°) | Latitude (°) | 1-s solutions | | | 30-s solutions | | | 24-h static solutions | | |
|---|---|---|---|---|---|---|---|---|---|---|---|
| | | | N (mm) | E (mm) | U (mm) | N (mm) | E (mm) | U (mm) | N (mm) | E (mm) | U (mm) |
| HGC8 | 121.6051 | 24.1157 | | | | -87.5 ± 4.2 | 2.8 ± 3.8 | 29.7 ± 10.6 | | | |
| HGC9 | 121.6128 | 23.9902 | | | | 469.0 ± 14.2 | 41.3 ± 12.9 | 150.5 ± 32.0 | | | |
| HUAL | 121.6135 | 23.9754 | 414.1 ± 4.3 | 146.3 ± 5.4 | 42.3 ± 16.2 | 446.7 ± 9.7 | 156.5 ± 8.2 | 112.1 ± 27.0 | 432.0 ± 2.9 | 167.7 ± 7.0 | 59.2 ± 3.0 |
| HUAP | 121.7464 | 24.3090 | -16.8 ± 5.6 | 9.4 ± 6.3 | -23.1 ± 20.9 | 37.8 ± 21.6 | 17.4 ± 12.8 | 14.4 ± 58.6 | -77.6 ± 5.2 | 20.0 ± 3.4 | -31.1 ± 8.9 |
| NDH1 | 121.5956 | 23.9624 | -279.9 ± 1.9 | 25.3 ± 4.5 | -41.0 ± 9.7 | -283.8 ± 4.3 | 32.2 ± 4.7 | -17.1 ± 14.8 | | | |
| NDH3 | 121.5653 | 23.9955 | -112.5 ± 1.8 | -120.7 ± 4.9 | 64.9 ± 10.8 | -130.8 ± 5.9 | -119.3 ± 4.4 | 45.5 ± 13.9 | | | |
| NDH4 | 121.5199 | 23.9168 | -48.1 ± 2.0 | -81.1 ± 4.4 | 8.9 ± 11.0 | -40.6 ± 4.7 | -88.5 ± 2.9 | 23.9 ± 7.9 | | | |
| NDH5 | 121.6181 | 24.0100 | 170.3 ± 2.1 | 58.5 ± 4.9 | 74.1 ± 12.2 | 166.4 ± 3.9 | 55.4 ± 3.0 | 112.9 ± 7.1 | | | |
| NDHU | 121.5508 | 23.8972 | -28.6 ± 2.7 | -90.0 ± 4.2 | 16.4 ± 9.1 | -45.7 ± 8.6 | -83.0 ± 6.2 | 69.9 ± 19.4 | -64.5 ± 3.3 | -94.7 ± 1.8 | 32.6 ± 2.8 |
| PEPU | 121.6103 | 24.0179 | -270.0 ± 6.6 | -41.4 ± 12.7 | 88.3 ± 10.5 | -273.9 ± 17.3 | -68.6 ± 23.1 | 65.2 ± 61.7 | -286.1 ± 7.4 | -53.9 ± 3.4 | 51.2 ± 7.9 |
| SCHN | 121.6516 | 24.1278 | -94.2 ± 4.1 | 6.4 ± 2.3 | -22.6 ± 10.5 | | | | -136.1 ± 7.7 | 29.7 ± 8.7 | -30.9 ± 7.1 |
| SICH | 121.6544 | 24.1257 | -94.8 ± 3.8 | 3.2 ± 4.2 | -32.6 ± 11.4 | -65.7 ± 6.2 | 14.4 ± 4.2 | 45.6 ± 14.8 | | | |
| SOFN | 121.5982 | 23.8703 | 103.5 ± 4.4 | -17.5 ± 4.6 | 41.8 ± 9.7 | 84.7 ± 12.9 | 8.2 ± 14.0 | 75.6 ± 65.4 | | | |
| YENL | 121.6018 | 23.9035 | 192.0 ± 3.0 | -16.8 ± 4.0 | -52.8 ± 11.0 | 204.3 ± 4.8 | -24.5 ± 5.4 | -31.0 ± 14.6 | 188.5 ± 2.3 | -12.9 ± 2.0 | -34.4 ± 5.7 |

Milun fault also show significant northeastward horizontal displacement of 175 and 470 mm and uplift of about 100 and 150 mm, respectively. In contrast, on the footwall of the Milun fault, the GPS station PEPU recorded a horizontal displacement of about 280 mm trending to the southwest and a coseismic uplift of about 70 mm. The coseismic motion indicates Milun fault is a left-lateral strike-slip faults with reverse motion which is consistent with the reverse sense based on geological investigations and kinematic behavior of coseismic deformation of the 1951 $M_L$ 7.1 Hualien earthquake (e.g., Hsu 1962, 1971; Bonilla 1975, 1977; Yamaguchi and Ota 2004).

Further south, the GPS station YENL located on the hanging wall of the Lingding fault measured a horizontal displacement of about 200 mm trending to the northwest and a coseismic subsidence of 35 mm; the station NDHU located on the footwall of the Lingding Fault shows a coseismic uplift behavior, the vertical motion of these two stations is inconsistent with the kinematic behavior of the Lingding fault considered as a NS-striking east-dipping reverse fault with left-lateral slip component from geological investigations (Chen et al. 2007) and geodetic measurements during the interseismic period (Chen 1974; Yu and Liu 1989; Yu and Kuo 2001). Thus an unknown west-dipping fault with left-lateral strike-slip component could be triggered during this $M_w$ 6.4 Hualien event.

### 3.2 D-InSAR Result

D-InSAR is complementary with GPS observations but with more spatial extensive measurements. The main surface deformation with numerous of fringes in interferograms can be observed around the Milun fault and northern Lingding fault. In contrast, only two fringes (representing 56 mm in range difference) are observed from the ascending orbit of Sentinel-1 near the epicenter (Fig. 3). After phase unwrapping, a significant shortening along the LOS can be observed on the hanging wall of the Milun fault in the descending orbit, which implies coseismic uplift and/or eastward motion in this area. Significant shortening along the LOS is presented on the footwall of the Lingding fault in the ascending orbit, suggesting a coseismic uplift and/or a westward motion dominated in this area (Fig. 4).

One of the limitations of for detecting deformation with InSAR is that it only provides one component of the surface deformation along line of sight (LOS) towards the satellite. Previous studies have investigated to map surface deformation in three dimensions by using multiple interferograms with different imaging geometries (e.g., Wright et al. 2004; Biggs et al. 2007). In general, the north-south component of surface deformation is always the most difficult to detect with the lager errors than the signals using data from near-polar orbiting satellites. If we assume north-south component is negligible, the eastward and vertical motion can be well determined. However, the coseismic deformation along the NE-striking left-lateral strike-slip Milun fault is not the case for the assumption of negligible north-south component, because the north-south component of deformation is significant. For measuring coseismic deformation the, the pixel offset tracking techniques have been applied to characterize the coseismic deformation of the Milun fault (Huang and Huang 2018; Kuo et al. 2019; Yen et al. 2019). These studies provide the valuable information for coseismic deformation along and across the left-lateral strike-slip dominated Milun fault. However, the accuracy of the sub-pixel correlation method highly depends on pixel size. Previous studies suggested that the sub-pixel correlation method using a pair of SPOT panchromatic images could provide fault slip measurements with an accuracy of 0.1 pixel in theory (Michel and Avouac 2002; Dominguez et al. 2003; Leprince et al. 2007). For the coseismic deformation calculated by using offsets tracking with sub-pixel correlation of SAR amplitude (Simons et al. 2002; Fialko et al. 2005; Pathier et al. 2006; Elliott et al. 2007; Huang and Huang 2018), however this technique does not directly provide horizontal displacement. It measures track-parallel (azimuth offsets) and track-perpendicular (range offsets) displacement components (Fialko et al. 2005), thus the east-west and north-south component could be inferred according to azimuth and range offsets. In addition, the accuracy of the displacement filed inferred from offset tracking technique is affected by topographic complexity of the study area and ionospheric distortions. That could be the reason why Huang and Huang (2018) didn't incorporate the offset tracking coseismic deformation filed near the Milun fault in their inversion of rupture model of the Hualien.

To better characterize the coseismic deformation pattern around the Milun and Lingding faults, we combined ascending and descending interferograms to obtain E-W and vertical displacement components (Fig. 5) by following equations:

$$E_{component} = \frac{LOS^{(des)} \cdot \cos(\theta_{asc}) - LOS^{(asc)} \cdot \cos(\theta_{des})}{\cos(\alpha_{des}) \cdot \sin(\theta_{des}) \cdot \cos(\theta_{asc}) + \cos(\alpha_{asc}) \cdot \sin(\theta_{asc}) \cdot \cos(\theta_{des})} \quad (1)$$

$$U_{component} = \frac{LOS^{(asc)} + E_{component} \cdot \cos(\alpha_{asc}) \cdot \sin(\theta_{asc})}{\cos(\theta_{asc})} \quad (2)$$

Where $\theta$ is the incidence angle and $\alpha$ is intersection angle between the trace of satellite (Heading Angle) and the north; *asc* represents ascending orbit while *des* represents descending orbit (Table 1). Results obtained from ALOS-2 and Sentinel-1 both show that the uplift area is mainly located on the hanging wall of the Milun fault with the maximum uplift of 55 mm. Meanwhile, minor coseismic uplift is also observed on both sides of the Lingding fault. The maximum coseismic subsidence, reaching to 35 mm, is located in the southmost

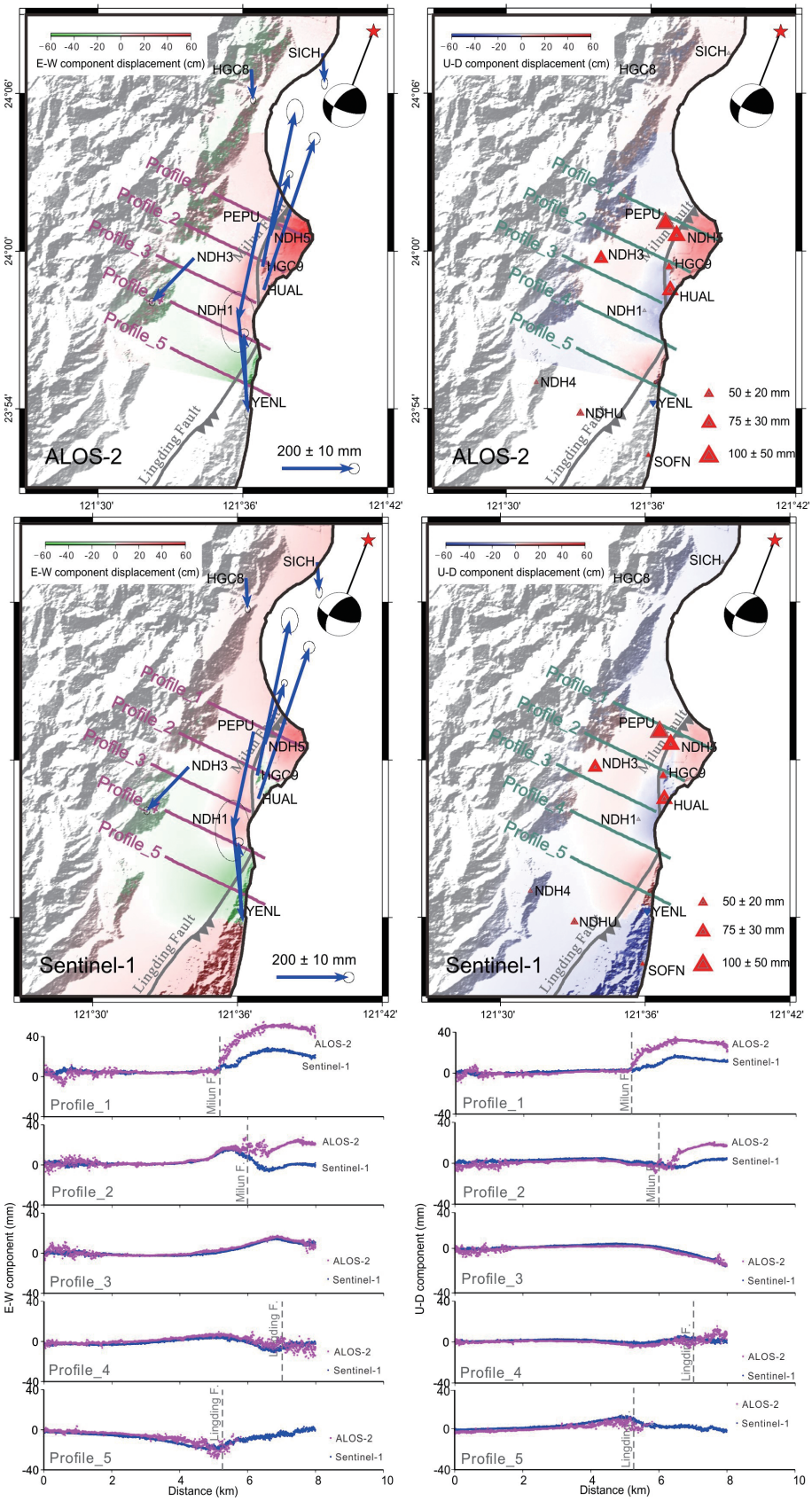


Fig. 5. E-W and vertical component coseismic deformation and profiles across the main deformation area. Red color represents eastward surface rupture and uplift; green color represents westward movement and blue color represents subsidence. Blue arrows represent the GPS horizontal displacements and solid triangles indicate the vertical movements of cGPS stations. Pink dots in profiles represent the deformation signals extracted from ALOS-2, and blue dots represent the deformation signals extracted from Sentinel-1.

footwall of the Milun fault. In general, the coseismic uplift obtained using ALOS-2 data is larger compared to that from Sentilnel-1 data. This difference could have resulted from the ionosphere effect of ALOS-2 pairs.

Five profiles across the main deformation area are shown in Fig. 5. Significant coseismic uplift is observed in the hanging wall of the Milun fault along profiles 1 and 2 in both ALOS-2 and Sentinel-1 data. Furthermore, coseismic uplift is larger in the northern part of the hanging wall of the Milun fault compared to that in the southern part of the hanging wall. On the other hand, moderate coseismic uplift can be observed on the footwall of the Lingding fault, this observation is inconsistent with the kinematic behavior for a NE-striking and east-dipping left-lateral strike-slip fault with a reverse component (Chen et al. 2007). It is worth noting that significant coseismic subsidence observed in an area separating the Milun fault and Lingding fault. For E-W coseismic component, the significant eastward motion of about 55 and 30 mm are observed in ALOS-2 and Sentinel-1 images on the hanging wall of the Milun fault, respectively (Profiles 1 and 2 in left panel of Fig. 5). Although InSAR technique could not well detect along-track coseismic displacement (subparallel to the strike of the Milun fault), however if we decompose of the fault-parallel displacement revealed by the optical image correlation of aerial photos (the maximum offset of 1 m from Kuo et al. 2019) and field survey (the maximum offset of ~ 77 cm from Huang et al. 2019), the eastward motions are consistent with our results. The main westward coseismic motion dominates in the footwall of the Lingding fault, which is consistent with the observation from GPS stations showing a NW motion in this area. Thus, the coseismic uplift and westward motion also imply that an unknown west-dipping fault system might exist close to the Lingding fault.

## 4. DISCUSSION

### 4.1 Hourly Solution

24-hour static solution at GPS station HUAP and SCHN located at northern Hualien show a significant subsidence of 31 mm (Table 2). However, estimates of vertical motion from the kinematic solutions do not show the same feature (subsidence of 20 mm in 1-s and uplift of 14 mm in 30-s solutions). Thus, we divide daily data into 6 hours' intervals for static positioning. Here we use two stations HUAP and HUAL to show the time series of 6-hours solutions prior to, during and post the 0204 $M_w$ 6.0 event and the 0206 event (Fig. 6). The subsidence and southeastward displacement could only be observed in stations (HGC1~7 and HUAP) located northwest to the epicenter of the 0204 $M_w$ 6.0 event. In contrast, coseismic displacement of 0204 $M_w$ 6.0 event is insignificant at the station HUAL in the city of Hualien. Thus, we suggest that the coseismic vertical motion of HUAP is contaminated by the 0204 event and kinematic solutions will be useful to distinguish coseismic displacements of multi-events occurred in a short time span compared to the daily solutions.

### 4.2 Seismic Ground Motion - Peak Ground Displacement

Following the study of magnitude scaling properties of peak ground displacement (Melgar et al. 2015), Eq. (1) is used to determine peak ground displacement, where N(t), E(t), and U(t) are the north, east, and vertical displacement in each epoch, respectively.

$$PGD = \max\left[\sqrt{N(t)^2 + E(t)^2 + U(t)^2}\right] \quad (3)$$

The peak ground displacement (PGD) derived from GPS waveform in Stations HUAL and PEPU are shown in Fig. 7, the PGD is about 1135 and 386 mm, respectively. We also use the waveform data from two strong motion seismometers HWA019 and HWA028 close to GPS stations HUAL and PEPU to compare with the GPS displacement waveform. The good agreement from two data set suggests the high-rate GPS measurements could be used as strong motion data. In addition, we also calculated the arrival time of the PGD estimated from GPS waveforms. Surprisingly, the earliest arrival time of 12 s recorded at the both sides of the Milun fault from 4 GPS stations (PEPU, NDH5, NDH1, and HUAL) and shows a southward increase (Fig. 8). However, two GPS stations SCHN and SICH located in Hsinchen near the epicenter of the 0206 event revealed an arrival time of the PGD of about 15 s. If we assume the S wave velocity of 6.5 km $s^{-1}$, the shear wave should arrival at these two stations in about only 3 s. This implies that the PGD observed in the epicenter area and along the Milun fault should resulted from the triggered Milun fault after the mainshock.

### 4.3 Candidate of Unknown West-Dipping Fault

Yang et al. (2018) used three faults to explain the deformation pattern derived from D-InSAR and GPS after the 0206 event. They suggested a NE-striking and west-dipping fault subparallel to the east-dipping Lingding fault responsible for the observed deformation pattern. An alternative fault model proposed by Lee et al. (2019) by using joint inversion of teleseismic and GPS data suggesting a fault-to-fault jumping rupture. They implied that both the slip on Milun and Lingding faults were triggered by 0206 event. They suggested that the initial rupture started from a N-S striking and west-dipping fault and propagated southward with a high rupture speed, then the rupture then jumped to the shallower east-dipping Milun fault. The rupture jumped again to the east-dipping Lingding fault. Wen et al. (2019) also suggested the mainshock ruptured southward on two

fault segments, with a weak but fast imitation in the main west dipping segment and low yet significant slip on shallow east-dipping segment. Moreover, Huang and Huang (2018) suggested this event initiated from a south-dipping fault in offshore near Hsinchen ridge, and slip transferred in to the main west-dipping oblique fault and the east-dipping Milun fault in order by applied joint inversion of seismic, GPS, InSAR, and leveling data. They consider the main west-dipping main fault belongs to a different fault system that is different from the east-dipping Longitudinal Valley fault system (LVF). The west-dipping fault and easting-dipping LVF could be very close in the shallow depth, but close in space at the shallowest part. However, Yen et al. (2019) used 3D displacement field and numerical modeling to characterize the coseismic behavior of the Milun and Lingding faults. They suggest that the Milun and Lingding faults merge downward into a fault zone, thus they inferred that the Milun and Lingding faults belong to same fault zone with similar kinematic behavior during the Hualien event. This suggestion is quite different with previous models which suggest the west-dipping fault is the major seismogenic fault or trigger rupture around the Lingding fault during the Hualien event (Huang and Huang 2018; Yang et al. 2018; Lee et al. 2019; Wen et al. 2019).

In addition, the $M_L$ 6.4 Ruisui earthquake occurred in the Central Range of eastern Taiwan in 2013 also gave a clue for the existence of NE-striking and west-dipping seismogenic fault in Central Range. The seismogenic fault responsible for the surface deformation was a NNE-SSW-striking and west-dipping fault with a major slip located at a depth between 10 and 20 km (Lee et al. 2014). The seismogenic fault was considered as the central segment of the

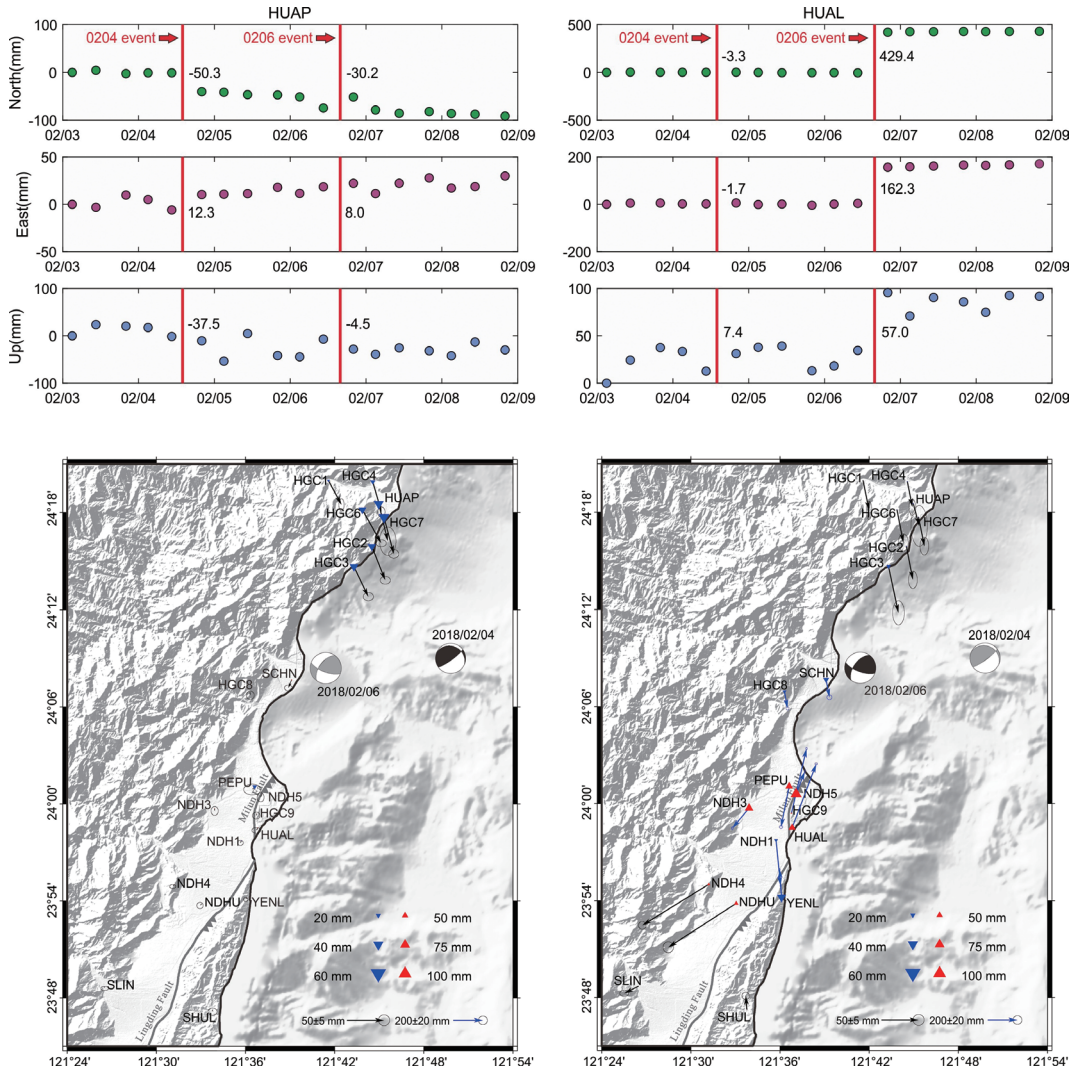


Fig 6. Upper-panel: time-series of cGPS stations HGC7 and HUAL. Two gray lines represent occurring time of the two main shocks of the 0204 $M_w$ 6.0 and 0206 $M_w$ 6.4 events. Numbers represent the coseismic displacements in three components of the two earthquakes. Lower-panel: coseismic displacement of 6-hours solutions of continuous GPS stations for the 0204 (left) and 0206 (right) events. Blue and black arrows represent the GPS horizontal displacements and solid triangles indicate the vertical movements of cGPS stations.

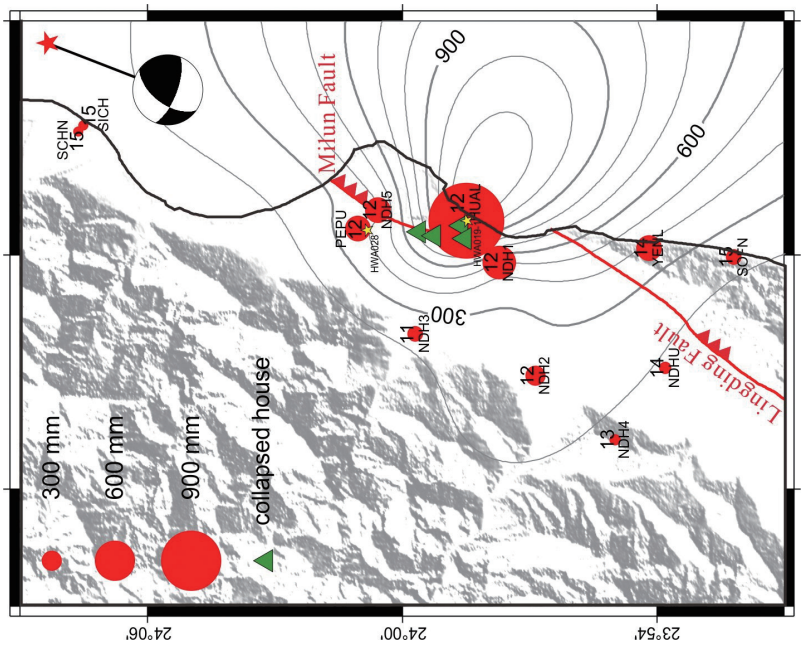


Fig. 8. Peak ground displacement estimation based on epoch-by-epoch solution from high-rate (1-Hz) GPS data. The size of red circles represents the amplitudes of the PGD for each station, and the number represents the arrival time of the PGD in second. The contour lines of PGD values are shown in gray lines.

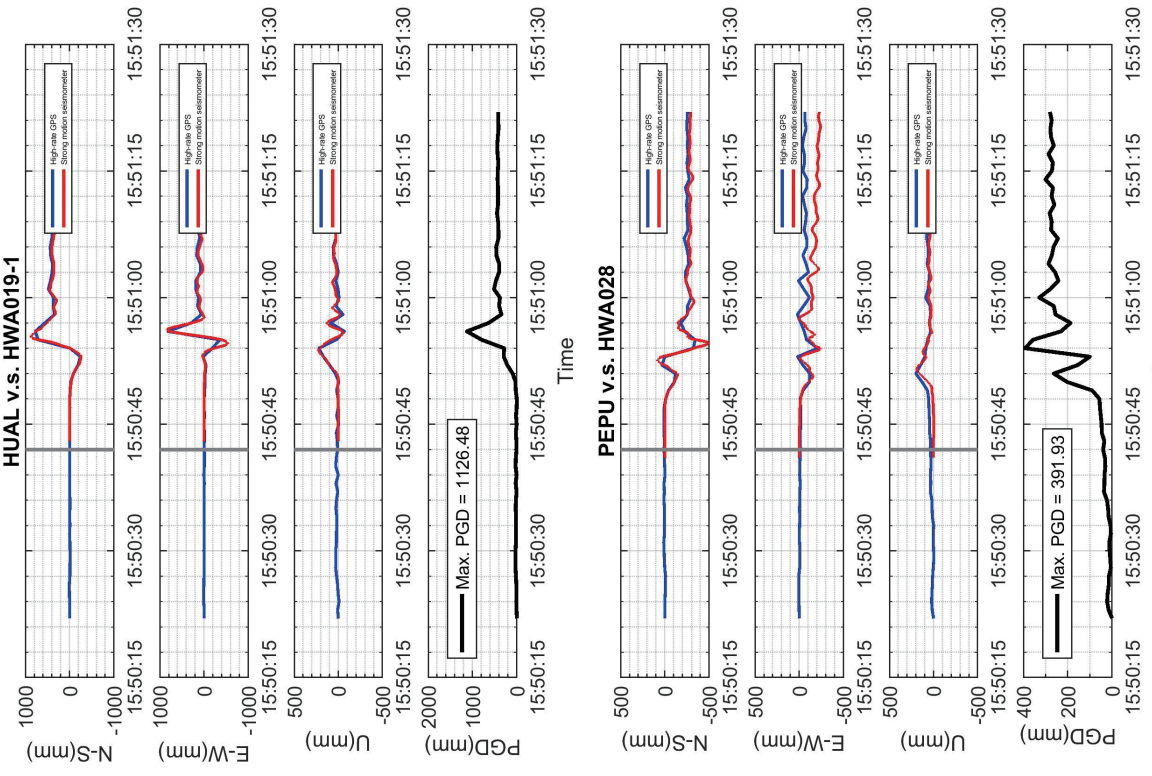


Fig 7. Comparison of GPS displacement waveform in N-S, E-W and vertical (U) components with adjacent strong motion stations and the Peak Ground Displacement (PGD) derived from GPS waveforms used in this study. Locations of GPS station and strong motion stations are shown in Fig. 8.

Central Range fault, where fault tip could propagate to a shallow depth intersecting with the NE-striking and east-dipping Longitudinal Valley fault (Fig. 9, profile BB'). The west-dipping Central Range Fault has been also observed along the northern segment near the Hualien area as revealed by a study of repeating earthquakes (Chen et al. 2009). This west-dipping Central Range Fault is also proposed cutting across the Lingding fault by geological profile (Fig. 9, modified from Chen 2016). Based on tomography data, focal mechanism and background seismicity, this NE-striking and west-dipping Central Range fault could extend offshore up to the epicenter area of the 0206 event (Wen-Shan Chen, personal communication), this tectonic model could support the possible candidate of the west-dipping fault which was triggered during the 0206 $M_w$ 6.4 Hualien event.

## 5. CONCLUSION

In this study, we investigate the coseismic deformation field associated with the 2018 $M_w$ 6.4 Hualien earthquake using GPS data and four tracks of InSAR measurement. The GPS-derived coseismic deformation based on kinematic and static positioning show significant coseismic deformation occurred along the Milun fault and extended southward to the northern part of the Lingding fault. The InSAR-derived coseismic deformation field shows similar features with most deformation located on the both sides of the Milun fault and in the footwall of the Lingding fault. In summary, the major coseismic deformation zone occurred along the Milun fault and in the footwall of the Lingding fault far from the epicenter. Additionally, the arrival time of

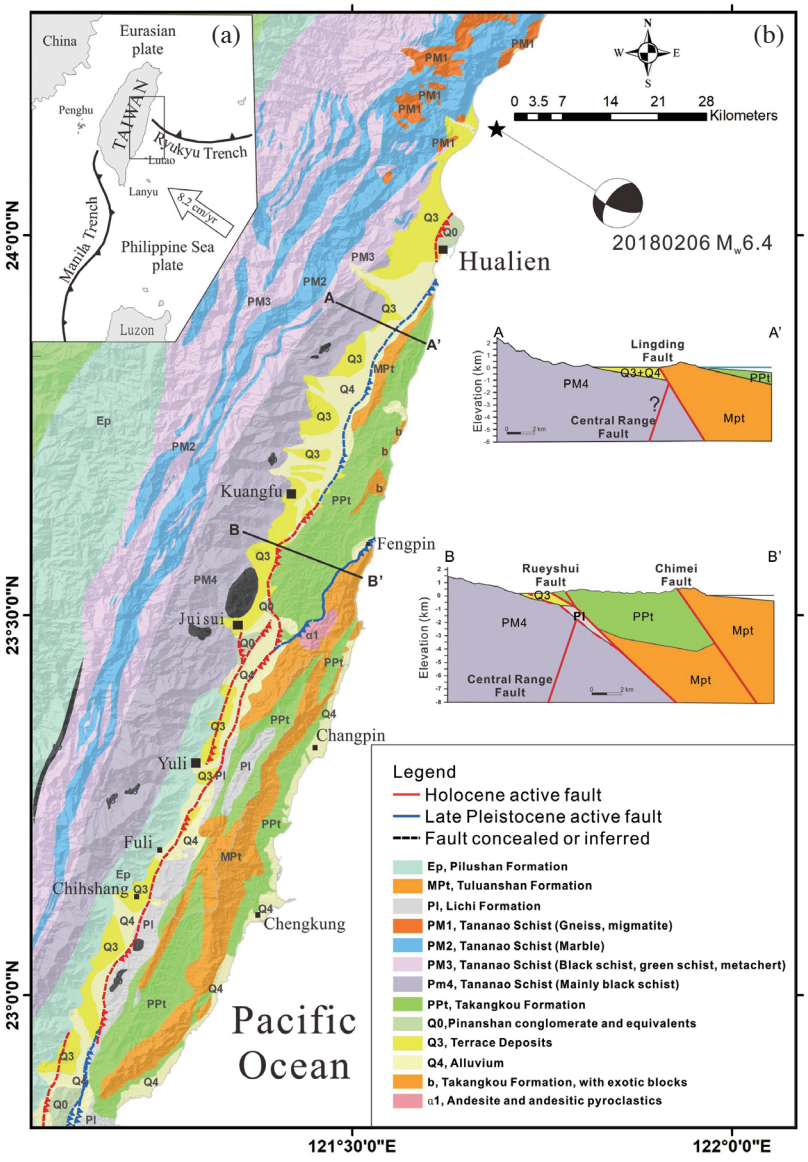


Fig. 9. (a) Simplified tectonic framework of eastern Taiwan and location of the geological map. (b) Simplified geological map of eastern Taiwan with two geological profiles across the Lingding and Ruisui fault (modified from Chen 2016).

the peak ground motion based on high-rate GPS waveforms indicate a long delay compared to a typical wave propagation velocity, suggesting the hypothesis of multi-fault slip triggering during the 0206 event.

**Acknowledgements** We are grateful to two anonymous reviewers, Stephane Dominguez and Guest Editor Ruey-Juin Rau for constructive comments that led us to significantly improve the manuscript. The authors would like to express their sincere gratitude to the generous provision of continuous GPS data by CWB, MOI, WRA, and National Dong Hwa University in Taiwan as well as precise ephemerides of GPS satellites by the IGS community is greatly appreciated. ALOS-2 SAR images were provided by the Japan Aerospace Exploration Agency (JAXA) under the ALOS-2 RA6 Project (PI No. 3255), and the Sentinel-1 SAR images were provided by the European Space Agency (ESA). This work is partially supported by the Ministry of Science and Technology in Taiwan under the grant 107-2116-M-002-016, and IESAS-2375.

## REFERENCES

Biggs, J., T. Wright, Z. Lu, and B. Parsons, 2007: Multi-interferogram method for measuring interseismic deformation: Denali Fault, Alaska. *Geophys. J. Int.*, **170**, 1165-1179, doi: 10.1111/j.1365-246X.2007.03415.x. [Link]

Bock, Y., L. Prawirodirdjo, and T. I. Melbourne, 2004: Detection of arbitrarily large dynamic ground motions with a dense high-rate GPS network. *Geophys. Res. Lett.*, **31**, L06604, doi: 10.1029/2003GL019150. [Link]

Bonilla, M. G., 1975: A review of recently active faults in Taiwan. U.S. Geological Survey Open-File Report, 75-41, 58 pp.

Bonilla, M. G., 1977: Summary of Quaternary faulting and elevation changes in Taiwan. *Mem. Geol. Soc. China*, **2**, 43-55.

Chang, Y.-H., S.-H. Hung, and Y.-L. Chen, 2019: A fast algorithm for automatic phase picker and event location: Application to the 2018 Hualien earthquake sequences. *Terr. Atmos. Ocean. Sci.*, **30**, 435-448, doi: 10.3319/TAO.2018.12.23.01. [Link]

Chen, C. W. and H. A. Zebker, 2000: Network approaches to two-dimensional phase unwrapping: Intractability and two new algorithms. *J. Opt. Soc. Am.*, **17**, 401-414, doi: 10.1364/josaa.17.000401. [Link]

Chen, C.-Y., 1974: Verification of the north-northeastward movement of the Coastal Range, eastern Taiwan, by re-triangulation. *Bull. Geol. Surv. Taiwan*, **24**, 119-123. (in Chinese)

Chen, K. H., R.-J. Rau, and J.-C. Hu, 2009: Variability of repeating earthquake behavior along the Longitudinal Valley fault zone of eastern Taiwan. *J. Geophys. Res.*, **114**, B05306, doi: 10.1029/2007JB005518. [Link]

Chen, P.-F., Y.-L. Chen, P.-L. Su, Y.-D. Peng, and L.-F. Chen, 2019: Understanding the 6 February 2018, Hualien earthquake sequence through catalog compilation. *Terr. Atmos. Ocean. Sci.*, **30**, 399-409, doi: 10.3319/TAO.2018.11.15.02. [Link]

Chen, W.-S., 2016: Introduction of Geology in Taiwan. Geol. Soc. China, Taipei, 250 pp. (in Chinese)

Chen, W.-S., I.-C. Yen, K. P. Fengler, C. M. Rubin, C.-C. Yang, H.-C. Yang, H.-C. Chang, C.-W. Lin, W.-H. Lin, Y.-C. Liu, and Y.-H. Lin, 2007: Late Holocene paleoearthquake activity in the middle part of the Longitudinal Valley fault, eastern Taiwan. *Earth Planet. Sci. Lett.*, **264**, 420-437, doi: 10.1016/j.epsl.2007.09.043. [Link]

Dach, R., U. Hugentobler, P. Fridez, and M. Meindl, 2007: Bernese GPS Software Version 5.0, Astronomical Institute, University of Bern.

Dominguez, S., J.-P. Avouac, and R. Michel, 2003: Horizontal coseismic deformation of the 1999 Chi-Chi earthquake measured from SPOT satellite images: Implications for the seismic cycle along the western foothills of central Taiwan. *J. Geophys. Res.*, **108**, doi: 10.1029/2001JB000951. [Link]

Elliott, J. L., J. T. Freymueller, and B. Rabus, 2007: Coseismic deformation of the 2002 Denali fault earthquake: Contributions from synthetic aperture radar range offsets. *J. Geophys. Res.*, **112**, B06421, doi: 10.1029/2006JB004428. [Link]

Farr, T. G., P. A. Rosen, E. Caro, R. Crippen, R. Duren, S. Hensley, M. Kobrick, M. Paller, E. Rodriguez, L. Roth, D. Seal, S. Shaffer, J. Shimada, J. Umland, M. Werner, M. Oskin, D. Burbank, and D. Alsdorf, 2007: The shuttle radar topography mission. *Rev. Geophys.*, **45**, RG2004, doi: 10.1029/2005RG000183. [Link]

Fialko, Y., D. Sandwell, M. Simons, and P. Rosen, 2005: Three-dimensional deformation caused by the Bam, Iran, earthquake and the origin of shallow slip deficit. *Nature*, **435**, 295-299, doi: 10.1038/nature03425. [Link]

Hamling, I. J., S. Hreinsdóttir, K. Clark, J. Elliott, C. Liang, E. Fielding, N. Litchfield, P. Villamor, L. Wallace, T. J. Wright, E. D'Anastasio, S. Bannister, D. Burbidge, P. Denys, P. Gentle, J. Howarth, C. Mueller, N. Palmer, C. Pearson, W. Power, P. Barnes, D. J. A. Barrell, R. Van Dissen, R. Langridge, T. Little, A. Nicol, J. Pettinga, J. Rowland, and M. Stirling, 2017: Complex multifault rupture during the 2016 $M_w$ 7.8 Kaikōura earthquake, New Zealand. *Science*, **356**, eaam7194, doi: 10.1126/science.aam7194. [Link]

Herring, T. A., R. W. King, and S. C. McClusky, 2009: Introduction to GAMIT/GLOBK, Release 10.35, Mass. Inst. of Technol., Cambridge.

Hsu, M.-T., 1971: Seismicity of Taiwan and some related problems. *Bull. Intern. Inst. Seismol. Earthq. Eng.*, **8**, 41-160.

Hsu, T.-L., 1962: Recent faulting in the longitudinal valley of eastern Taiwan. *Mem. Geol. Soc. China*, **1**, 95-102.

Huang, M.-H. and H.-H. Huang, 2018: The Complexity of the 2018 $M_w$ 6.4 Hualien Earthquake in East Taiwan. *Geophys. Res. Lett.*, **45**, 13249-13257, doi: 10.1029/2018GL080821. [Link]

Huang, M.-H., H. Tung, E. J. Fielding, H.-H. Huang, C. Liang, C. Huang, and J.-C. Hu, 2016: Multiple fault slip triggered above the 2016 $M_w$ 6.4 MeiNong earthquake in Taiwan. *Geophys. Res. Lett.*, **43**, 7459-7467, doi: 10.1002/2016GL069351. [Link]

Huang, S.-Y., J.-Y. Yen, B.-L. Wu, I.-C. Yen, and R. Y. Chuang, 2019: Investigating the Milun Fault: The coseismic surface rupture zone of the 2018/02/06 $M_L$ 6.2 Hualien earthquake, Taiwan. *Terr. Atmos. Ocean. Sci.*, **30**, 311-335, doi: 10.3319/TAO.2018.12.09.03. [Link]

Kuo, Y.-T., Y. Wang, J. Hollingsworth, S.-Y. Huang, R. Y. Chuang, C.-H. Lu, Y.-C. Hsu, H. Tung, J.-Y. Yen, and C.-P. Chang, 2019: Shallow fault rupture of the Milun fault in the 2018 $M_w$ 6.4 Hualien earthquake: A high-resolution approach from optical correlation of Pléiades satellite imagery. *Seismol. Res. Lett.*, **90**, 97-107, doi: 10.1785/0220180227. [Link]

Kuo-Chen, H., Z.-K. Guan, W.-F. Sun, P.-Y. Jhong, and D. Brown, 2019: Aftershock sequence of the 2018 $M_w$ 6.4 Hualien earthquake in eastern Taiwan from a dense seismic array data set. *Seismol. Res. Lett.*, **90**, 60-67, doi: 10.1785/0220180233. [Link]

Le Béon, M., M.-H. Huang, J. Suppe, S.-T. Huang, E. Pathier, W.-J. Huang, C.-L. Chen, B. Fruneau, S. Baize, K. E. Ching, and J.-C. Hu, 2017: Shallow geological structures triggered during the $M_w$ 6.4 Meinong earthquake, southwestern Taiwan. *Terr. Atmos. Ocean. Sci.*, **28**, 663-681, doi: 10.3319/TAO.2017.03.20.02. [Link]

Lee, S.-J., H.-H. Huang, J. B. H. Shyu, T.-Y. Yeh, and T.-C. Lin, 2014: Numerical earthquake model of the 31 October 2013 Ruisui, Taiwan, earthquake: Source rupture process and seismic wave propagation. *J. Asian Earth Sci.*, **96**, 374-385, doi: 10.1016/j.jseaes.2014.09.020. [Link]

Lee, S.-J., T.-C. Lin, T.-Y. Liu, and T.-P. Wong, 2019: Fault-to-fault jumping rupture of the 2018 Mw 6.4 Hualien earthquake in eastern Taiwan. *Seismol. Res. Lett.*, **90**, 30-39, doi: 10.1785/0220180182. [Link]

Leprince, S., S. Barbot, F. Ayoub, and J.-P. Avouac, 2007: Automatic and precise orthorectification, coregistration, and subpixel correlation of satellite images, application to ground deformation measurements. *IEEE Trans. Geosci. Remote Sensing*, **45**, 1529-1558, doi: 10.1109/TGRS.2006.888937. [Link]

Lin, K.-C., J.-C. Hu, K.-E. Ching, J. Angelier, R.-J. Rau, S.-B. Yu, C.-H. Tsai, T.-C. Shin, and M.-H. Huang, 2010: GPS crustal deformation, strain rate, and seismic activity after the 1999 Chi-Chi earthquake in Taiwan. *J. Geophys. Res.*, **115**, B07404, doi: 10.1029/2009JB006417. [Link]

Lin, K.-C., B. Delouis, J.-C. Hu, J.-M. Nocquet, and L. Mozziconacci, 2016: Reassessing the complexity of the rupture of the 2010 Jia-Shian Earthquake ($M_w$ 6.2) in Southwestern Taiwan by inverting jointly teleseismic, strong-motion and CGPS data. *Tectonophysics*, **692**, 278-294, doi: 10.1016/j.tecto.2015.09.015. [Link]

Lin, Y.-S., R. Y. Chuang, J.-Y. Yen, Y.-C. Chen, Y.-T. Kuo, B.-L. Wu, S.-Y. Huang, and C.-J. Yang, 2019: Mapping surface breakages of the 2018 Hualien earthquake by using UAS photogrammetry. *Terr. Atmos. Ocean. Sci.*, **30**, 351-366, doi: 10.3319/TAO.2018.12.09.02. [Link]

Malavieille, J., S. E. Lallemand, S. Dominguez, A. Deschamps, C.-Y. Lu, C.-S. Liu, P. Schnuerle, J. Angelier, J. Y. Collot, B. Deffontaines, M. Fournier, S. K. Hsu, J. P. Le Formal, S. Y. Liu, J. C. Sibuet, N. Thareau, F. Wang, and the ACT (Active Collision in Taiwan) Scientific Crew, 2002: Arc-continent collision in Taiwan: New marine observations and tectonic evolution. In: Byrne, T .B. and C.-S. Liu (Eds.), Geology and Geophysics of an Arc-Continent Collision, Taiwan, GSA Special Papers, Geological Society of America, Vol. 358, 187-211, doi: 10.1130/0-8137-2358-2.187. [Link]

Melgar, D., B. W. Crowell, J. Geng, R. M. Allen, Y. Bock, S. Riquelme, E. M. Hill, M. Protti, and A. Ganas, 2015: Earthquake magnitude calculation without saturation from the scaling of peak ground displacement. *Geophys. Res. Lett.*, **42**, 5197-5205, doi: 10.1002/2015GL064278. [Link]

Michel, R. and J.-P. Avouac, 2002: Deformation due to the 17 August 1999 Izmit, Turkey, earthquake measured from SPOT images. *J. Geophys. Res.*, **107**, doi: 10.1029/2000JB000102. [Link]

Nikolaidis, R. M., Y. Bock, P. J. de Jonge, P. Shearer, D. C. Agnew, and M. Van Domselaar, 2001: Seismic wave observations with the Global Positioning System. *J. Geophys. Res.*, **106**, 21897-21916, doi: 10.1029/2001jb000329. [Link]

Pathier, E., E. J. Fielding, T. J. Wright, R. Walker, B. E. Parsons, and S. Hensley, 2006: Displacement field and slip distribution of the 2005 Kashmir earthquake from SAR imagery. *Geophys. Res. Lett.*, **33**, L20310, doi: 10.1029/2006GL027193. [Link]

Rosen, P. A., E. Gurrola, G. F. Sacco, and H. Zebker, 2012: The InSAR scientific computing environment. EUSAR 2012, Proc. 9th European Conference on Synthetic Aperture Radar, Nuremberg, Germany, 730-733.

Shyu, J. B. H., K. Sieh, Y.-G. Chen, and C.-S. Liu, 2005: Neotectonic architecture of Taiwan and its implications

for future large earthquakes. *J. Geophys. Res.*, **110**, B08402, doi: 10.1029/2004jb003251. [Link]

Simons, M., Y. Fialko, and L. Rivera, 2002: Coseismic deformation from the 1999 $M_w$ 7.1 Hector Mine, California, earthquake as inferred from InSAR and GPS observations. *Bull. Seismol. Soc. Am.*, **92**, 1390-1402, doi: 10.1785/0120000933. [Link]

Tian, S., P. Gardoni, and W. Yuan, 2019: Coseismic deformation of the 6 February 2018 $M_w$ 6.2 Hualien Earthquake based on strong-motion recordings. *Seismol. Res. Lett.*, **90**, 108-117, doi: 10.1785/0220180235. [Link]

Tsai, M.-C., S.-B. Yu, T.-C. Shin, K.-W. Kuo, P.-L. Leu, C.-H. Chang, and M.-Y. Ho, 2015: Velocity field derived from Taiwan continuous GPS array (2007 - 2013). *Terr. Atmos. Ocean. Sci.*, **26**, 527-556, doi: 10.3319/TAO.2015.05.21.01(T). [Link]

Webb, F. H. and J. F. Zumberge, 1997: An Introduction to GIPSY/OASIS II, JPL Publication D-11088.

Wen, Y.-Y., S. Wen, Y.-H. Lee, and K.-E. Ching, 2019: The kinematic source analysis for 2018 $M_w$ 6.4 Hualien, Taiwan earthquake. *Terr. Atmos. Ocean. Sci.*, **30**, 377-387, doi: 10.3319/TAO.2018.11.15.03. [Link]

Wright, T. J., B. E. Parsons, and Z. Lu, 2004: Toward mapping surface deformation in three dimensions using InSAR. *Geophys. Res. Lett.*, **31**, L01607, doi: 10.1029/2003GL018827. [Link]

Wu, B.-L., J.-Y. Yen, S.-Y. Huang, Y.-T. Kuo, and W.-Y. Chang, 2019: Surface deformation of 0206 Hualien earthquake revealed by the integrated network of RTK GPS. *Terr. Atmos. Ocean. Sci.*, **30**, 301-310, doi: 10.3319/TAO.2019.05.27.01. [Link]

Yamaguchi, M. and Y. Ota, 2004: Tectonic interpretations of Holocene marine terraces, east coast of Coastal Range, Taiwan. *Quat. Int.*, **115-116**, 71-81, doi: 10.1016/S1040-6182(03)00097-1. [Link]

Yang, Y.-H., J.-C. Hu, H. Tung, M.-C. Tsai, Q. Chen, Q. Xu, Y.-J. Zhang, J.-J. Zhao, G.-X. Liu, J.-N. Xiong, J.-Y. Wang, B. Yu, C.-Y. Chiu, and Z. Su, 2018: Co-Seismic and Postseismic Fault Models of the 2018 Mw 6.4 Hualien Earthquake Occurred in the Junction of Collision and Subduction Boundaries Offshore Eastern Taiwan. *Remote Sens.*, **10**, doi: 10.3390/rs10091372. [Link]

Yen, J.-Y., C.-H. Lu, R. J. Dorsey, H. Kuo-Chen, C.-P. Chang, C.-C. Wang, R.-Y. Chuang, Y.-T. Kuo, C.-Y. Chiu, Y.-H. Chang, F. Bovenga, and W.-Y. Chang, 2019: Insights into seismogenic deformation during the 2018 Hualien, Taiwan, earthquake sequence from InSAR, GPS, and modeling. *Seismol. Res. Lett.*, **90**, 78-87, doi: 10.1785/0220180228. [Link]

Yu, S.-B. and C.-C. Liu, 1989: Fault creep on the central segment of the Longitudinal Valley Fault, eastern Taiwan. *Proc. Geol. Soc. China*, **32**, 209-231.

Yu, S.-B. and L.-C. Kuo, 2001: Present-day crustal motion along the Longitudinal Valley Fault, eastern Taiwan. *Tectonophysics*, **333**, 199-217, doi: 10.1016/s0040-1951(00)00275-4. [Link]